

Core–shell MoO₃–MoS₂ Nanowires for Hydrogen Evolution: A Functional Design for Electrocatalytic Materials

Zhebo Chen,[†] Dustin Cummins,[‡] Benjamin N. Reinecke,[†] Ezra Clark,[‡] Mahendra K. Sunkara,[‡] and Thomas F. Jaramillo^{*,†}

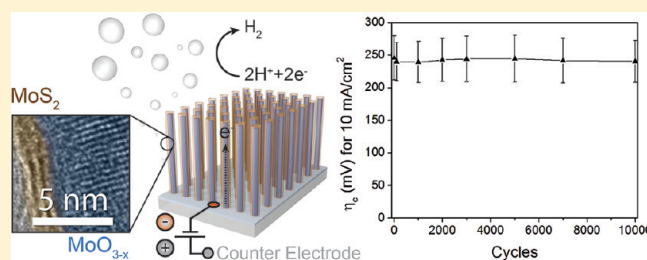
[†]Department of Chemical Engineering, Stanford University, Stanford, California 94305, United States

[‡]Department of Chemical Engineering, University of Louisville, Louisville, Kentucky 40292, United States

S Supporting Information

ABSTRACT: We synthesize vertically oriented core–shell nanowires with substoichiometric MoO₃ cores of ~20–50 nm and conformal MoS₂ shells of ~2–5 nm. The core–shell architecture, produced by low-temperature sulfidization, is designed to utilize the best properties of each component material while mitigating their deficiencies. The substoichiometric MoO₃ core provides a high aspect ratio foundation and enables facile charge transport, while the conformal MoS₂ shell provides excellent catalytic activity and protection against corrosion in strong acids.

KEYWORDS: Electrochemistry, catalysis, molybdenum sulfide, nanowires, hydrogen evolution



Electrocatalyst development has become increasingly important as a number of energy technologies rely upon electrochemical conversion reactions.^{1,2} Electrocatalytic hydrogen production by water splitting is one example; this process could potentially address the needs for the sustainable production of fuels and for solar energy storage in a manner that is renewable and carbon-free.^{2,3} In contrast to widely utilized steam reformed hydrogen, electrocatalytically produced hydrogen offers much lower carbon monoxide content, which can mitigate the poisoning effect that often decreases operational activity of platinum-based catalysts currently used in hydrogen fuel cells.^{4,5} Several device configurations can potentially enable solar driven water electrolysis, including coupled photovoltaic (PV) electrolyzers,^{6,7} integrated PV electrolyzers,^{8,9} and photoelectrochemical (PEC) water splitting cells.^{1,10–13} Research into PEC water splitting, in particular, has experienced large growth in recent years. However, the development of a single material that can meet the requirements of high solar photon-to-current conversion, catalytic activity, and stability represents a significant unmet challenge. One strategy is to decouple the various requirements by utilizing multiple materials. Enhancements in the activity for silicon photocathodes by depositing hydrogen evolution catalysts on the Si surface, for example, have already been demonstrated using this approach.^{14,15} The hydrogen evolution catalyst is a key component which needs to be able to drive current densities that match the solar photon flux at low overpotentials while remaining stable in the chosen electrolyte. In this work, we describe our efforts to develop a high aspect ratio hydrogen evolution electrocatalyst based on MoS₂.

In order to circumvent conductivity limitations in MoS₂¹⁶ that might hinder charge transport in a high aspect ratio structure, we

have designed an electrode architecture consisting of core–shell nanowires with a vertical orientation. By combining a conductive core consisting of substoichiometric MoO₃ ~20–50 nm in diameter, with a conformal MoS₂ shell of thickness ~2–5 nm, we have successfully created a high aspect ratio structure that can enable charge transport over large distances (micrometers) with high catalytic activity and stability in strong acids. This electrode architecture design takes advantage of the best properties of each material while mitigating their deficiencies. The architecture is particularly relevant to recently reported arrays of microwire semiconductors (e.g., Si) for PEC^{14,15} and more universally applicable to enabling electrocatalytic materials with insufficient long-range conductivity, for example, water oxidation catalysts consisting of poorly conducting metal oxides.¹⁷

State-of-the-art hydrogen evolution catalysts currently consist of platinum or platinum-based materials^{18–20} due to their negligible overpotential and excellent kinetics for driving the hydrogen evolution reaction (HER). However, the widespread use of platinum may be limited by its scarcity and high cost,²¹ and thus development of non-noble metal alternatives remains attractive. Such alternatives typically include nickel or nickel-based materials,^{22–26} which operate in alkaline electrolytes. Their long-term stability in strong acids, however, remains a significant challenge. As a result, these catalysts are difficult to integrate into systems that operate in acid, such as photoelectrochemical cells containing tungsten oxide,^{27–29} p-type silicon,^{15,30} or gallium–indium-phosphide.^{31–33}

Received: June 18, 2011

Revised: August 24, 2011

Published: September 06, 2011

Molybdenum disulfide (MoS_2) is a layered chalcogenide material that shows poor activity for the HER in bulk form.¹⁶ However, nanoparticles of MoS_2 synthesized in ultrahigh vacuum (UHV) were shown to exhibit excellent activity for the HER, activity that correlated with the number of exposed edge sites which were thus determined to be the catalytically active sites.³⁴ Several studies have since presented excellent HER activity on various forms of MoS_2 and its analogues.^{35–38} As a result of these studies, there is now growing interest to use MoS_2 as a catalyst directly attached to a variety of substrates, such as photocathodes^{39,40} or simply as a standalone cathode to complete a photoanode device. Syntheses of nanostructured MoS_2 oftentimes employ thermal H_2S treatments, sometimes at temperatures greater than 700 °C in order to fully form nested fullerene structures.^{41,42} Such high temperatures limit the substrates which can be used due to the highly reactive nature of H_2S . More recent studies of single-layer MoS_2 clusters were conducted using lower sulfidization temperatures of 400–550 °C which, for electrochemical studies, required the use of inert supports, such as gold or carbon, to avoid a loss in substrate conductivity during the sulfidization process.^{34,35} Solution phase synthesis of a highly active MoS_2 has also been investigated,³⁸ and electrochemical synthesis of a highly active MoS_3 analogue has even been achieved at room temperature.³⁷ Vapor phase routes to synthesis still remain an attractive avenue of exploration, particularly in the production of high-quality interfaces with desired substrates. Our study elucidates the controlled nanometer-scale growth of conformal MoS_2 coatings from MoO_3 at temperatures as low as 200 °C, enabling the use of sulfidization-sensitive substrates, such as fluorine-doped tin oxide (FTO), a conductive substrate desirable for its electrochemical stability over a wide range of potentials and pH values.

As a standalone cathode, MoS_2 needs to be driven at relevant current densities while maintaining stability. This has been recently achieved with MoS_2 supported on reduced graphene oxide in a rotating disk configuration.³⁸ Alternatively, a high aspect ratio, high surface area morphology can be employed to increase activity, similar to Raney nickel. The anisotropic conductivity of MoS_2 poses a challenge for high surface area structures as the conductivity of MoS_2 is poor along certain crystallographic directions.¹⁶ To circumvent this limitation, we have developed a core–shell MoO_3 – MoS_2 nanowire catalyst with the following design criteria in mind: (1) a partially reduced MoO_3 core with high conductivity, (2) a MoS_2 shell (surface) with high catalytic activity and stability in acids, and (3) a morphology of vertically aligned core–shell nanowires to provide a high aspect ratio and high surface area. This material constitutes a MoS_2 -based HER catalyst that is capable of driving current densities that match the solar photon flux at low overpotential, while remaining stable under rigorous potential cycling in a strong acid with $\text{pH} < 1$.

Hot-wire chemical vapor deposition (HWCVD) is used to synthesize MoO_3 nanowires (see Supporting Information) with a general vertical orientation, as observed by scanning electron microscopy (SEM) images in Figure 1. There are no noticeable differences in the external nanowire morphology before or after (Figure 1a or b, respectively) sulfidization in 10% H_2S /90% H_2 at 200 °C. At sulfidization temperatures of 300 °C and above, some nanowires appear sharper at their tips and can be described as having a more blade-like (grass-like) morphology. Morphological changes are most pronounced at an even higher temperature of 700 °C, as shown in Figure 1e, where the widths of some of the nanowires are noticeably larger, while others appear to have an

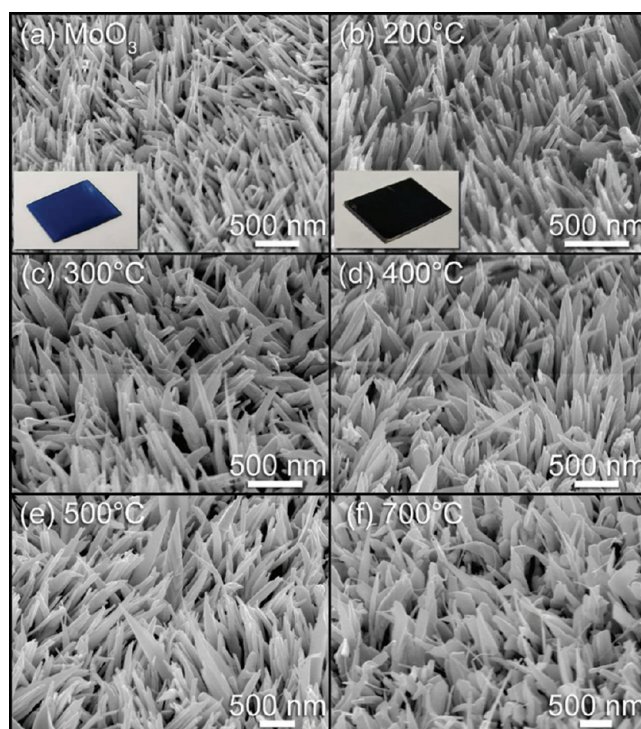


Figure 1. External morphology of nanowires. SEM images taken at 45° from normal of (a) unsulfidized MoO_3 nanowires and nanowires sulfidized at (b) 200 °C, (c) 300 °C, (d) 400 °C, (e) 500 °C, and (f) 700 °C. Insets for (a) and (b) show photographs of the respective samples (physical dimensions of 2×3 cm).

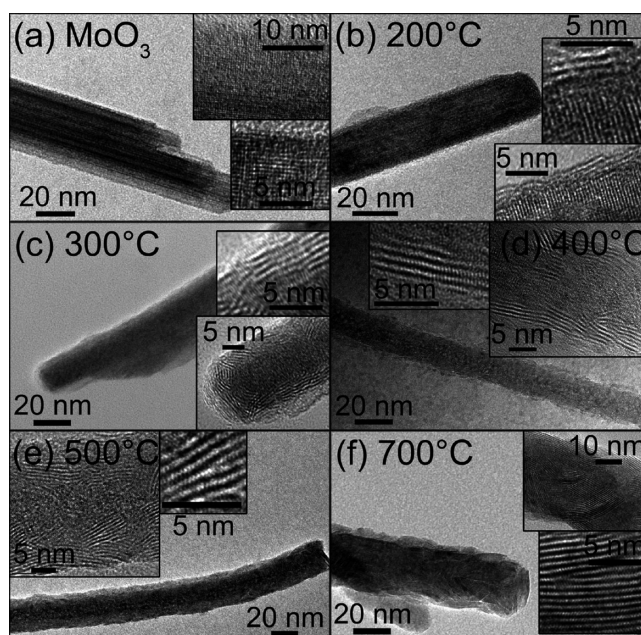


Figure 2. Internal morphology of nanowires. TEM images of (a) unsulfidized MoO_3 nanowires and nanowires sulfidized at (b) 200 °C, (c) 300 °C, (d) 400 °C, (e) 500 °C, and (f) 700 °C.

even thinner, more whisker-like morphology. The thin whiskers could perhaps suggest some extent of mass transfer between the

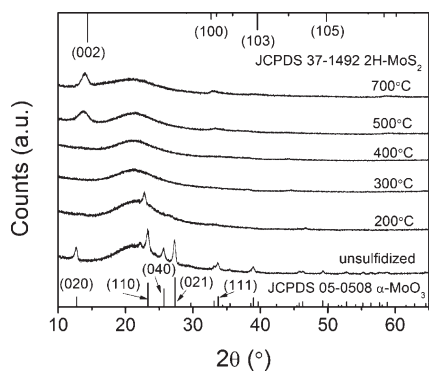


Figure 3. Bulk composition of the nanowires. X-ray diffraction spectra of Mo nanowires on amorphous quartz sulfidized at various temperatures. The reference spectra for α - MoO_3 (JCPDS 05-0508) and 2H- MoS_2 (JCPDS 37-1492) are shown at the bottom and top, respectively, with several major peaks labeled. A broad peak associated with the quartz substrate is visible for all samples at approximately 22° .

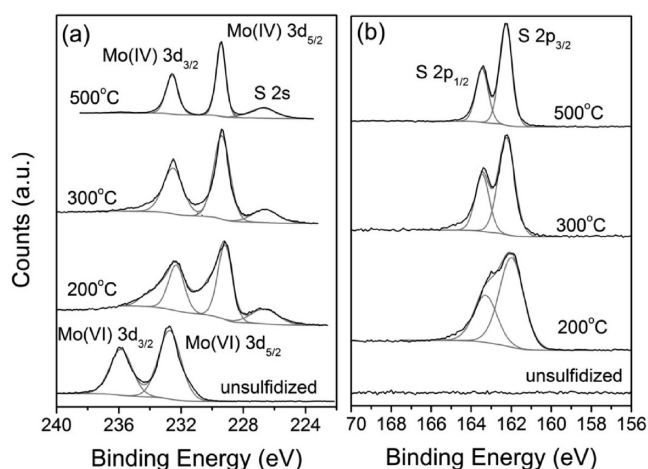


Figure 4. Surface composition of nanowires. XPS spectra of Mo nanowires before and after sulfidization at various temperatures showing the (a) Mo 3d and S 2s peaks and (b) S 2p peaks. Fitted peaks are shown in gray lines. Peak intensities are scaled for clarity.

individual nanowires at higher temperatures, although sintering of multiple smaller nanowires into a larger nanowire may also be occurring.

The structure of MoS_2 consists of S–Mo–S layers separated by a van der Waals gap, as observed in the transmission electron microscopy (TEM) images shown in Figure 2b–f, in which the layers appear only at the outer radius of the nanowires and reveal a core–shell morphology. The MoS_2 layers exhibit curvature and branching, resulting in layer-to-layer spacings of 6.4 Å on average (Figure S1a, Supporting Information), slightly larger than the bulk layer-to-layer spacing of 6.1 Å.¹⁶ The atoms within the layers exhibit an average spacing of 2.7 Å (Figure S1a, Supporting Information) consistent with previous TEM studies of MoS_2 along the (100) plane.⁴³ The exact arrangement of the S–Mo–S layers leads to the possible formation of 3 different polytypes (Figure S2, Supporting Information): 1T (tetragonal), 2H (hexagonal), or 3R (rhombohedral),^{16,44} though the spacing between particular layers along the $[00l]$ direction (where l is 1, 2, or 3 depending on the tetrahedral, hexagonal, or rhombohedral

polytype, respectively) remains unchanged. With higher sulfidization temperatures, the thickness of the shell layer increases (Figure S3, Supporting Information) accompanied by a noticeable increase in the size of the polycrystalline grains. At the highest reaction temperature of 700 °C, the layered structure appears to penetrate completely through the core of the nanowire.

The X-ray diffraction data shown in Figure 3 reveal that the unsulfidized nanowires made by HWCVD consist of orthorhombic α - MoO_3 . When subjected to 200 °C sulfidization, the data show that crystallinity is still present, albeit at a diminished level. This crystallinity is also observed in the TEM image shown in Figure 2b. When sulfidized at higher temperatures 300 °C and above, all peaks corresponding to the molybdenum oxide have disappeared, indicating a lack of long-range order of that phase. Meanwhile, a peak corresponding to the (00 l) reflection of MoS_2 appears at 13.9° (6.4 Å). This peak is shifted from the bulk reference value of 14.4° (6.1 Å) for the (002) reflection from 2H- MoS_2 and consistent with the average value (6.4 Å) measured from the TEM images. The small size of the observed polycrystalline grains is further reflected in the large full width at half-maximum (fwhm) of the (00 l) peak, which is approximately 1.5° when sulfidized at 500 °C, though the fwhm decreases to 1.0° when sulfidized at 700 °C. Per the Scherrer equation, this decrease in fwhm indicates an increase in the average crystallite size, consistent with the TEM images in Figure 2.

X-ray photoelectron spectroscopy (XPS) was used to investigate the chemical states of Mo and S in the surface region of the nanowires, as shown in Figure 4. The binding energy of the Mo 3d_{5/2} electron peak for the unsulfidized nanowires (232.7 eV) in Figure 4a reveal a 6+ oxidation state consistent with MoO_3 . Once exposed to sulfidization at temperatures as low as 200 °C, however, much of the signal from the Mo 3d_{5/2} peak shifts to a lower binding energy (229.2 eV) indicative of a 4+ oxidation state, along with the appearance of a S 2s peak at 226.7 eV, as shown in Figure 4b. Signals from higher oxidation states remain and contribute to a tailing of the Mo 3d signal into higher binding energies, since the sulfidization process does not extend deeply beyond the surface of the nanowires at this temperature, as observed in the TEM image of Figure 2b; the tailing spectra are likely due to a partial reduction of the 6+ oxide into 5+ and 4+ states. At sulfidization temperatures of 300 °C and above, the 4+ oxidation state represents the entirety of the observed signal since the oxide core lies beyond the surface detection limit of XPS. Examination of the S 2p_{3/2} peak at 162.2 eV shows that the sulfur exists entirely in a 2– oxidation state at all sulfidization temperatures, consistent with the formation of MoS_2 . In general, deconvolution of the inelastic scattering in the baseline signal leads to some error in peak fitting; however, where baseline errors are minimized due to the strong signal from the Mo 3d and S 2s peaks (at 500 °C), the quantification of the peak areas confirms a Mo:S ratio of 1:2, as calibrated using a bulk crystal of MoS_2 (SPI).

Electrochemical measurements of the nanowires were conducted in a three-electrode cell (see Supporting Information for details on setup). Cyclic voltammograms of nanowires sulfidized at various temperatures are shown in Figure 5a and b. Unsulfidized MoO_3 nanowires showed extreme instability under testing conditions, immediately producing a large cathodic corrosion peak that corresponded to a visible degradation of the nanowires from the surface of the substrate. This is expected behavior as the Pourbaix diagram of the Mo–O system indicates MoO_3 has a limited window of stability (only at anodic potentials and in

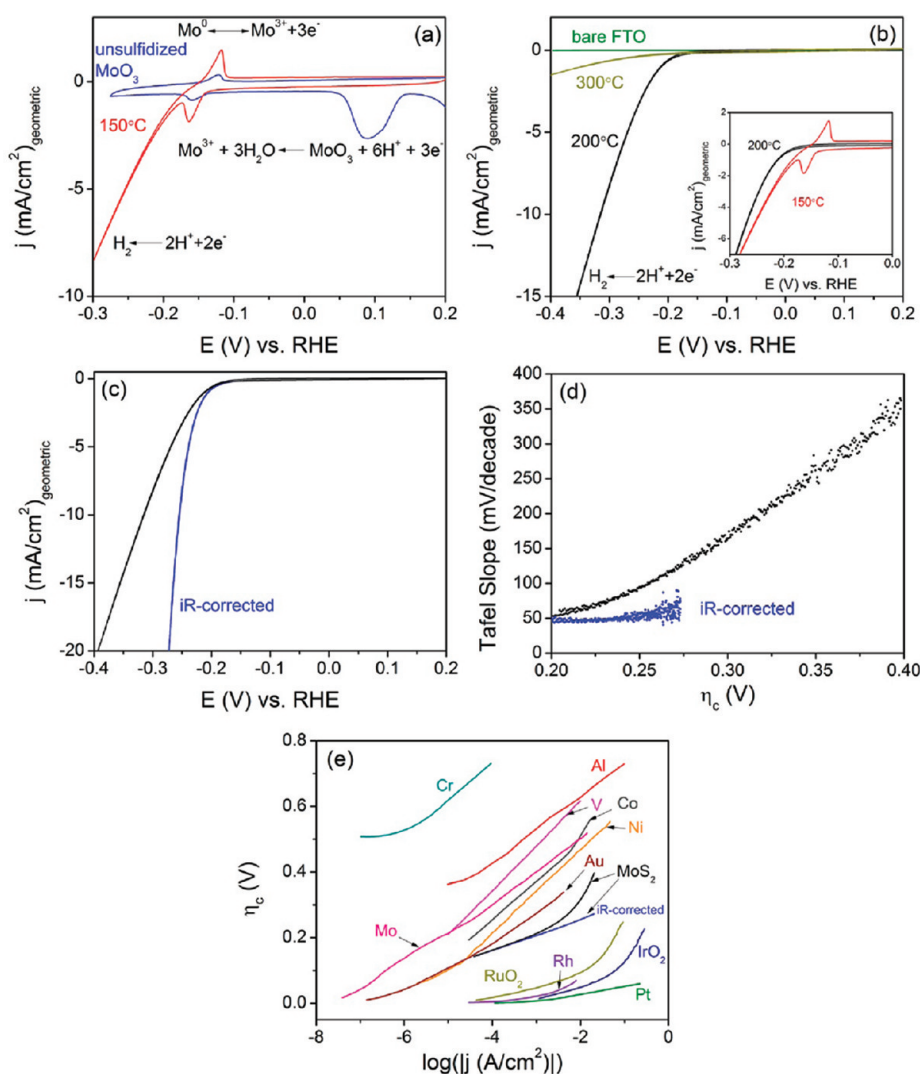


Figure 5. Electrochemical activity of nanowires. Cyclic voltammograms of unsulfidized nanowires and nanowires sulfidized at 150 °C are shown in plot (a). Nanowires sulfidized at 200 and 300 °C are shown in plot (b), along with a sweep of bare TEC15 FTO without nanowires that was sulfidized at 200 °C for reference. The inset in (b) shows a comparison between nanowires sulfidized at 150 and 200 °C. In plot (c), the activity of the nanowires sulfidized at 200 °C is presented with its *iR*-corrected data. The Tafel slope is shown in plot (d), which is produced from taking a derivative of the Tafel plot in (e). Included in plot (e) is comparison to digitized data of HER measurements at 25 °C of Pt wire in 1.0 M of H₂SO₄,⁵⁶ Au and Mo wires in 0.1 N of HCl,⁵¹ Rh wire in 0.01 N of HCl,⁵¹ Ni crystal in 1.0 M of HClO₄,²² Al wire in 0.5 N of H₂SO₄,⁵⁷ and Cr/V/Co wires in 1.0 N of H₂SO₄.⁵⁸

acidic media).⁴⁵ Nanowires sulfidized to temperatures as low as 150 °C initially showed an early onset for the HER (<0.2 V overpotential) but extremely poor stability (Figure S5, Supporting Information). The presence of a redox couple associated with an Mo³⁺/Mo⁰ transition as well as one associated with an MoO₃/Mo³⁺ transition, if scanned at slightly more anodic potentials (Figure S6, Supporting Information), indicated that the sulfur surface coverage was incomplete, resulting in the exposure of the core MoO₃ structural support to the acidic environment in which it is unstable. At a sulfidization temperature of 200 °C, however, these redox features were no longer visible, indicating complete surface coverage of the sulfide. The HER activity for nanowires sulfidized at 200 °C, despite having a slightly less favorable onset compared to nanowires sulfidized at 150 °C (inset of Figure 5b), remained stable under repeated cycling, as will be discussed further below. Sulfidization at a higher temperature of 300 °C resulted in a significant decrease in HER activity. Upon further

analysis by electrochemical impedance spectroscopy (Figure S7, Supporting Information), this was attributed to a loss of conductivity in the FTO substrate due to chemical changes within this higher temperature sulfidization environment (Figure S8, Supporting Information), although increased resistance from the thicker sulfide shell or from chemical changes to the MoO₃ core is also plausible. Further exploration of the thermal processing parameters, such as varying the ramp rate and soak time, may yield different results on the morphology of the nanowires and present an interesting opportunity for future study and optimization.

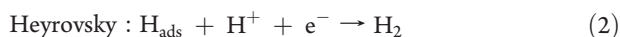
A typical cyclic voltammogram of nanowires sulfidized at 200 °C is shown in Figure 5c. The nanowires exhibit an onset for the HER at an overpotential of approximately 150–200 mV, consistent with earlier results seen for nanostructured MoS₂.^{34–36} The energetics of the HER reaction steps on MoS₂ have previously been studied by means of density functional theory (DFT) calculations.⁴⁶ It was shown that for a low coverage of

hydrogen atoms at the active MoS₂ edge sites, the hydrogen–sulfur bond is strong, leading to a thermodynamically downhill H adsorption step at any HER overpotential. In the low-overpotential region $\eta_c < 80$ mV, H coverage is low, and the S–H bond is too strong to produce (and release) molecular H₂. At higher overpotentials >80 mV, however, H coverage increases along the edge and in this higher-coverage state and at these potentials, all steps are thermodynamically downhill to produce molecular H₂. As H₂ is released, the local coverage is reduced once again, leaving open sites upon which more protons can adsorb and turnover into H₂. These calculations are consistent with the 150–200 mV onset of HER activity for the core–shell MoO₃–MoS₂ nanowires, particularly when considering the addition of reaction barriers which are sure to exist.

To gain more insight into the activity of the nanowires, a Tafel plot was constructed. The resulting Tafel slope is 50–60 mV/decade near the onset of current at 200 mV, but rises quickly with increasing overpotential, as shown by the black data points in Figure 5d. Examination of the series resistance components of the electrochemical cell using electrochemical impedance spectroscopy revealed the cause of the rising Tafel slope, a significant measured ohmic resistance of approximately 14 Ω , owing to a sum of the series resistances from the FTO substrate and the solution (Figure S9, Supporting Information). In order to elucidate the true kinetic activity of the nanowires, *iR*-corrected data is presented in Figure 5c–e.

Following a correction for the ohmic resistances, the cyclic voltammogram shows a steady Tafel slope as seen in Figure 5d, suggesting that correcting for losses from the substrate and solution resistance appears to have fully accounted for all ohmic losses in the system. While fully stoichiometric MoO₃ is an insulator that would contribute significant resistance, the MoO₃ nanowires synthesized by the HWCVD method exhibit a deep-blue color (inset of Figure 1a) indicative of a substoichiometric bulk composition arising from oxygen vacancies that absorb light in the green and red region of the visible spectrum (Figure S10c, Supporting Information). The absorption features remain after 200 °C sulfidization but are not observed at higher temperatures. These oxygen vacancies are known to enhance conductivity by several orders of magnitude.⁴⁷ In addition, the thermal treatment in the highly reducing atmosphere of H₂ further reduced the oxide, evidenced by the XPS measurements of the near-surface oxidation state shown in Figure 4. These reduced states are known to possess metallic conductivity.^{48–50} The thin layer of MoS₂, which is often a poor conductor due to its anisotropic conductivity,¹⁶ appears to contribute no significant resistance at this length scale; larger MoS₂ structures could potentially present significant and unavoidable ohmic losses, an issue circumvented by the core–shell MoO₃–MoS₂ nanowire design.

Mechanistically, three principal steps can participate in the conversion of 2H⁺ to H₂, commonly referred to as the Volmer (eq 1), the Heyrovsky (eq 2), and the Tafel (eq 3) steps.^{51,52}



Combinations of steps [eqs 1 and 2] or [eqs 1 and 3], i.e., Volmer–Heyrovsky or Volmer–Tafel, can lead to the production of molecular H₂. Experimentally measured Tafel slopes have

often been used to identify the HER mechanism and its rate-determining step (r.d.s.). The Tafel slope of 50–60 mV/decade measured in this work closely matches that measured on MoS₂ nanoparticles prepared in UHV,³⁴ suggesting a similarity in surface chemistry for these two catalysts despite differences in morphology and synthetic preparation.³⁴

Kinetic models of the HER, under a specific set of conditions, have shown that if the Volmer step is the r.d.s. a slope of ~ 120 mV/decade should result, while a rate-determining Heyrovsky or Tafel step should produce slopes of ~ 40 or ~ 30 mV/decade, respectively.^{20,51,52} While these values can be used as a guide in identifying HER mechanisms, one should bear in mind that those calculations are based on a strict set of assumptions that do not universally hold. For instance, the value of the transfer coefficients, α , of the elementary steps can vary for different materials and experimental conditions, or the surface coverage of adsorbed H might vary significantly as a function of applied potential. Multiple pathways can also occur in parallel with one another. Thus, identifying the HER mechanism based on Tafel slope analysis alone is not always clear, even on well-defined and thoroughly investigated materials such as Pt(111).^{20,53} For the case of nanostructured MoS₂, it is not surprising that a wide range of Tafel slopes have previously been observed depending on the catalyst preparation, ranging from 40 to 120 mV/decade.^{34,35,38} Ab initio models have recently emerged that provide insight into mechanistic aspects of HER catalysis on surfaces,^{54,55} enabling the future possibility for further elucidation of the HER mechanism on MoS₂.

Figure 5e is a compilation of HER activity data (per projected geometric area) for a representative number of different catalysts operating in a strong acid medium.^{18,22,51,56–58} For the sake of clarity, this is not an exhaustive compilation of HER catalyst materials. However, key precious and nonprecious metal catalysts are shown. The core–shell MoO₃–MoS₂ nanowires (denoted “MoS₂” in the figure) are highly active compared to other non-noble materials, particularly at higher current densities (>10 mA/cm²).

Even though the nanowires are already quite efficient, there may still be opportunities to improve upon this material design. The TEM images in Figure 2 show that the MoS₂ basal planes are for the most part parallel to the nanowire axis, exposing few MoS₂ edge sites at the surface of the nanowires. Increasing the proportion of edge sites at the surface could lead to improvements in performance. In order to assess the ceiling for further improvement, we first calculated an overall turnover frequency (TOF) of H₂/sec per MoS₂ (denoted simply as units of s^{−1}) by normalizing the HER current to the experimentally measured surface area of MoS₂. The MoS₂ surface area was determined by first measuring the total amount of MoS₂ on the nanowires as calculated from anodic dissolution titration measurements (Figure S11a, Supporting Information), and then dividing this value by the number of MoS₂ layers in the nanowire shell as observed in the TEM images (Figure 2 and Figure S3, Supporting Information). This calculation yields the exposed surface area of the MoS₂, from which a TOF, averaging over all sites including basal plane and edge sites, of approximately 4 s^{−1} at -0.272 V is calculated (*iR* corrected *E* at *j* = 20 mA/cm², see Supporting Information for details). For comparison, the inherent edge site TOF for MoS₂ was calculated at -0.272 V based on measurements on well-defined UHV-prepared MoS₂ nanoparticles: 680 or 1270 s^{−1} (sulfidized at 550 or 400 °C, respectively). This difference of a factor of $\sim 150 \times -300 \times$ in TOFs between the core–shell

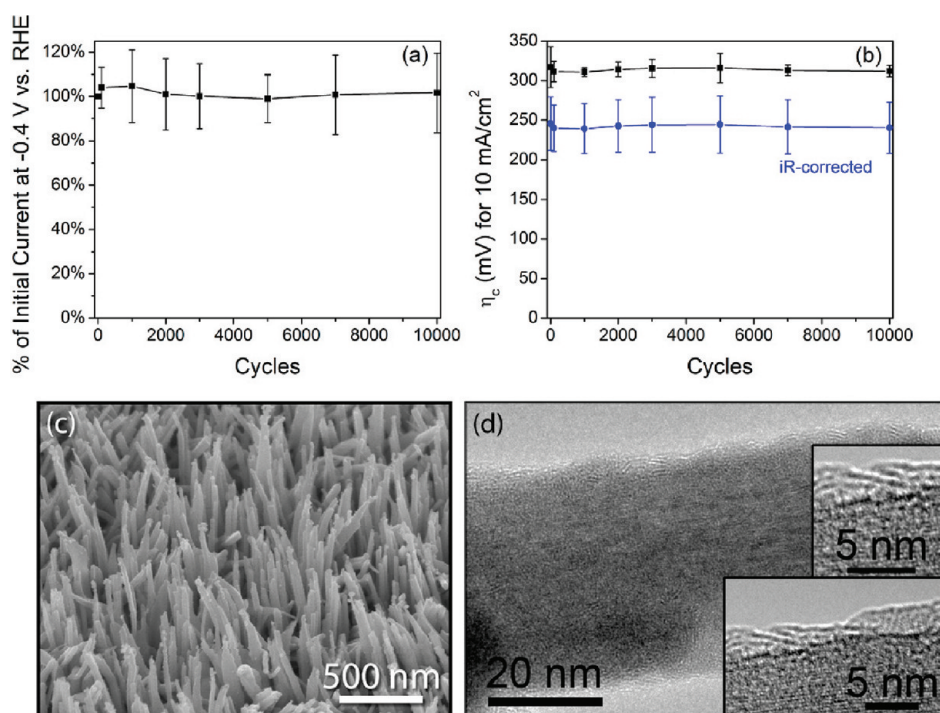


Figure 6. Electrochemical stability of the sulfidized nanowires in acid. Plot (a) shows the cycling stability of nanowires sulfidized at 200 °C, measured as current density at -0.4 V vs RHE, normalized to initial current density. Plot (b) shows the overpotential stability required to drive 10 mA/cm^2 with *iR* correction (blue circles) and without *iR* correction (black squares). Data points are an average of 3 samples, while error bars represent a 95% confidence interval (two standard deviations). SEM and TEM (c and d, respectively) images show the external and internal morphology of the nanowires after 10 000 potential cycles.

MoO₃–MoS₂ nanowire surface and the edge sites of UHV-prepared MoS₂ nanoparticles gives a quantitative measure of how few edge sites exist on the MoS₂ shell compared to basal plane sites. Thus, there may be an opportunity to improve significantly upon their activity by producing more edge sites on the MoS₂ shell. Previous studies have shown that a gentle oxidation of MoS₂, either thermally or electrochemically, can generate pits which expose more edge sites.^{59–61} Other techniques, such as Ar⁺ sputtering⁶² or plasma treatment, might also produce the desired defects.

Stability is a major concern for all catalysts. To probe HER stability in the acidic environment, long-term potential cycling stability of the nanowires was assessed by taking continuous cyclic voltammograms between -0.3 and 0.2 V vs RHE (not *iR* corrected) at 50 mV/s . This is analogous to the cycling tests formally used to assess the electrochemical stability of platinum catalysts for the oxygen reduction reaction as applied to fuel cells.⁶³ The upper voltage limit ($+0.2$ V) was chosen to be close to the measured open circuit potential of the nanowires. The lower voltage limit ($-0.3 \text{ V} = -0.24 \text{ V } iR\text{-corrected}$) was chosen since this is the potential at which the nanowires can drive approximately 8 mA/cm^2 of current density, a value that roughly corresponds to a 10% efficient solar-to-hydrogen conversion efficiency in a solar water splitting device.⁶⁴ In essence, cycling in this potential range serves to approximate the daily cycling that the nanowires may experience if integrated into a solar water splitting device. The open circuit potential represents the most anodic potential that the nanowires should experience, barring intentional anodic bias, which should be avoided for MoS₂ due to dissolution at more positive potentials (Figure S11, Supporting Information).³⁵ The stability cycling was paused at periodic

intervals in order to sample the activity of the nanowires using a slower scan rate of 5 mV/s to minimize contributions from current due to capacitance as well as over a slightly wider potential window (up to -0.4 V vs RHE, not *iR*-corrected).

The stability of the nanowires is shown in Figure 6 in two manners: as plots of (a) normalized current density at -0.4 V vs RHE (not *iR*-corrected) and (b) overpotential required to drive 10 mA/cm^2 versus the number of cycles. No degradation in electrochemical activity was observed from potential cycling up to 10 000 cycles. In fact, a slight increase in activity was observed compared to initial cycling of the nanowires, possibly due to the removal of surface contaminants or slight defecting of nonactive basal plane sites into active edge sites as a result of surface oxidation.^{59–61} Furthermore, SEM of the stability tested nanowires in Figure 6c show that they retained their morphology without any visible degradation even after 10 000 cycles. TEM further confirmed that the core–shell morphology remained intact (Figure 6d). To further elucidate the protective nature of the conformal MoS₂ shell, Figure S11b, Supporting Information, is an SEM image of the nanowires upon removal of the sulfide layer, in the absence of the MoS₂ shell, significant deformation is observed due to the severe instability of MoO₃ in acid medium.

We have developed core–shell MoO₃–MoS₂ nanowires that efficiently drive the HER with stability over thousands of potential cycles. The partially reduced MoO₃ serves as a highly nanostructured, conductive core, while the ultrathin and conformal MoS₂ shell serves as both a HER catalyst and a protective layer. If an ultrathin conformal coating of MoS₂ can protect MoO₃, which would otherwise dissolve under these conditions, there are likely promising potential applications of ultrathin MoS₂ films for stabilizing materials in corrosive acidic environments while

simultaneously providing effective catalysis for hydrogen evolution. More generally, this nanoscale design for an electrode architecture can be applied to a wide range of electrocatalyst materials where charge transport might hinder the development of high-aspect ratio structures.

■ ASSOCIATED CONTENT

S Supporting Information. Details of the HWCVD nanowire synthesis, additional TEM analysis, setup of electrochemical studies, impedance spectroscopy results, UV-Vis-NIR spectroscopy results, and assessment of turnover frequency using anodic dissolution titration measurements. This material is available free of charge via the Internet at <http://pubs.acs.org>.

■ AUTHOR INFORMATION

Corresponding Author

*E-mail: jaramillo@stanford.edu.

■ ACKNOWLEDGMENT

Early stage development of nanowire synthesis was a collaborative effort between T.F.J. supported by the U.S. Department of Energy, Office of Energy Efficiency and Renewable Energy, under subcontract NFT-9-88567-01 under prime contract no. DE-AC36-08GO28308 and M.K.S. supported under the DOE-EPSCoR program, DE-FG02-07ER46375. All physical and electrochemical characterization was supported as part of the Center on Nanostructuring for Efficient Energy Conversion (CNEEC) at Stanford University, an Energy Frontier Research Center funded by the U.S. Department of Energy, Office of Science, Office of Basic Energy Sciences under award number DE-SC0001060. We also thank Dr. Egill Skulason, Dr. Poul G. Moses, Dr. Jakob Kibsgaard, and Dr. Arnold Forman for helpful discussions.

■ REFERENCES

- Walter, M. G.; Warren, E. L.; McKone, J. R.; Boettcher, S. W.; Mi, Q. X.; Santori, E. A.; Lewis, N. S. *Chem. Rev.* **2010**, *110* (11), 6446–6473.
- Cook, T. R.; Dogutan, D. K.; Reece, S. Y.; Surendranath, Y.; Teets, T. S.; Nocera, D. G. *Chem. Rev.* **2010**, *110* (11), 6474–6502.
- Lewis, N. S.; Nocera, D. G. *Proc. Natl. Acad. Sci. U.S.A.* **2007**, *104* (50), 20142–20142.
- Das, S. K.; Reis, A.; Berry, K. J. *J. Power Sources* **2009**, *193* (2), 691–698.
- Elezovic, N. R.; Gajic-Krstajic, L.; Radmilovic, V.; Vracar, L.; Krstajic, N. V. *Electrochim. Acta* **2009**, *54* (4), 1375–1382.
- Gibson, T. L.; Kelly, N. A. *Int. J. Hydrogen Energy* **2008**, *33* (21), 5931–5940.
- Darras, C.; Sailler, S.; Thibault, C.; Muselli, M.; Poggi, P.; Hoguet, J. C.; Melscoet, S.; Pinton, E.; Grehant, S.; Gaily, F.; Turpin, C.; Astier, S.; Fontes, G. *Int. J. Hydrogen Energy* **2010**, *35* (8), 3322–3332.
- Licht, S.; Wang, B.; Mukerji, S.; Soga, T.; Umeno, M.; Tributsch, H. *J. Phys. Chem. B* **2000**, *104* (38), 8920–8924.
- Khaselev, O.; Bansal, A.; Turner, J. A. *Int. J. Hydrogen Energy* **2001**, *26* (2), 127–132.
- Fujishima, A.; Honda, K. *Nature* **1972**, *238* (5358), 37–38.
- Bak, T.; Nowotny, J.; Rekas, M.; Sorrell, C. C. *Int. J. Hydrogen Energy* **2002**, *27* (10), 991–1022.
- Kudo, A.; Miseki, Y. *Chem. Soc. Rev.* **2009**, *38* (1), 253–278.
- Gratzel, M. *Nature* **2001**, *414* (6861), 338–344.
- Hou, Y.; Abrams, B. L.; Vesborg, P. C. K.; Björketun, M. E.; Herbst, K.; Bech, L.; Setti, A. M.; Damsgaard, C. D.; Pedersen, T.; Hansen, O.; Rossmeisl, J.; Dahl, S.; Nørskov, J. K.; Chorkendorff, I. *Nat. Mater.* **2011**, *10* (6), 434–438.
- Boettcher, S. W.; Warren, E. L.; Putnam, M. C.; Santori, E. A.; Turner-Evans, D.; Kelzenberg, M. D.; Walter, M. G.; McKone, J. R.; Brunschwig, B. S.; Atwater, H. A.; Lewis, N. S. *J. Am. Chem. Soc.* **2011**, *133* (5), 1216–1219.
- Tributsch, H.; Bennett, J. C. *J. Electroanal. Chem.* **1977**, *81* (1), 97–111.
- Trasatti, S. *Electrochim. Acta* **1984**, *29* (11), 1503–1512.
- Schuldiner, S. *J. Electrochem. Soc.* **1959**, *106* (10), 891–895.
- Greeley, J.; Nørskov, J. K.; Kibler, L. A.; El-Aziz, A. M.; Kolb, D. M. *ChemPhysChem* **2006**, *7* (5), 1032–1035.
- Sheng, W. C.; Gasteiger, H. A.; Shao-Horn, Y. *J. Electrochem. Soc.* **2010**, *157* (11), B1529–B1536.
- Mineral Commodity Summaries*; U.S. Geological Survey: Reston, VA, 2011; <http://minerals.usgs.gov/minerals/pubs/mcs/2011/mcs2011.pdf>.
- Huq, A.; Rosenberg, A. J. *J. Electrochem. Soc.* **1964**, *111* (3), 270–278.
- Krstajic, N. V.; Jovic, V. D.; Gajic-Krstajic, L.; Jovic, B. M.; Antozzi, A. L.; Martelli, G. N. *Int. J. Hydrogen Energy* **2008**, *33* (14), 3676–3687.
- Birry, L.; Lasia, A. *J. Appl. Electrochem.* **2004**, *34* (7), 735–749.
- Endoh, E.; Otouma, H.; Morimoto, T.; Oda, Y. *Int. J. Hydrogen Energy* **1987**, *12* (7), 473–479.
- Marinovic, V.; Stevanovic, J.; Jugovic, B.; Maksimovic, M. *J. Appl. Electrochem.* **2006**, *36* (9), 1005–1009.
- Meda, L.; Tozzola, G.; Tacca, A.; Marra, G.; Caramori, S.; Cristino, V.; Bignozzi, C. A. *Sol. Energy Mater. Sol. Cells* **2010**, *94* (5), 788–796.
- Gaillard, N.; Cole, B.; Kaneshiro, J.; Miller, E. L.; Marsen, B.; Weinhardt, L.; Bar, M.; Heske, C.; Ahn, K. S.; Yan, Y. F.; Al-Jassim, M. M. *J. Mater. Res.* **2010**, *25* (1), 45–51.
- Bar, M.; Weinhardt, L.; Marsen, B.; Cole, B.; Gaillard, N.; Miller, E.; Heske, C. *Appl. Phys. Lett.* **2010**, *96* (3), 032107–1–032107–3.
- Boettcher, S. W.; Spurgeon, J. M.; Putnam, M. C.; Warren, E. L.; Turner-Evans, D. B.; Kelzenberg, M. D.; Maiolo, J. R.; Atwater, H. A.; Lewis, N. S. *Science* **2010**, *327* (5962), 185–187.
- Khaselev, O.; Turner, J. A. *Science* **1998**, *280* (5362), 425–427.
- Khaselev, O.; Turner, J. A. *J. Electrochem. Soc.* **1998**, *145* (10), 3335–3339.
- Deutsch, T. G.; Head, J. L.; Turner, J. A. *J. Electrochem. Soc.* **2008**, *155* (9), B903–B907.
- Jaramillo, T. F.; Jorgensen, K. P.; Bonde, J.; Nielsen, J. H.; Horch, S.; Chorkendorff, I. *Science* **2007**, *317* (5834), 100–102.
- Bonde, J.; Moses, P. G.; Jaramillo, T. F.; Nørskov, J. K.; Chorkendorff, I. *Faraday Discuss.* **2008**, *140*, 219–231.
- Jaramillo, T. F.; Bonde, J.; Zhang, J. D.; Ooi, B. L.; Andersson, K.; Ulstrup, J.; Chorkendorff, I. *J. Phys. Chem. C* **2008**, *112* (45), 17492–17498.
- Merki, D.; Fierro, S.; Vrubel, H.; Hu, X. *Chem. Sci.* **2011**, *2* (7), 1262–1267.
- Li, Y.; Wang, H.; Xie, L.; Liang, Y.; Hong, G.; Dai, H. *J. Am. Chem. Soc.* **2011**, *133* (19), 7296–7299.
- Zong, X.; Yan, H. J.; Wu, G. P.; Ma, G. J.; Wen, F. Y.; Wang, L.; Li, C. *J. Am. Chem. Soc.* **2008**, *130* (23), 7176–7177.
- Zong, X.; Wu, G. P.; Yan, H. J.; Ma, G. J.; Shi, J. Y.; Wen, F. Y.; Wang, L.; Li, C. *J. Phys. Chem. C* **2010**, *114* (4), 1963–1968.
- Margulis, L.; Salitra, G.; Tenne, R.; Talianker, M. *Nature* **1993**, *365* (6442), 113–114.
- Zak, A.; Feldman, Y.; Alperovich, V.; Rosentsveig, R.; Tenne, R. *J. Am. Chem. Soc.* **2000**, *122* (45), 11108–11116.
- Kisielowski, C.; Ramasse, Q. M.; Hansen, L. P.; Brorson, M.; Carlsson, A.; Molenbroek, A. M.; Topsoe, H.; Helveg, S. *Angew. Chem., Int. Ed.* **2010**, *49* (15), 2708–2710.
- Enyashin, A. N.; Bar-Sadan, M.; Sloan, J.; Houben, L.; Seifert, G. *Chem. Mater.* **2009**, *21* (23), 5627–5636.
- Pourbaix, M. *Atlas of electrochemical equilibria in aqueous solutions*; 2nd ed.; NACE International: Houston, TX, 1974.

- (46) Hinnemann, B.; Moses, P. G.; Bonde, J.; Jorgensen, K. P.; Nielsen, J. H.; Horch, S.; Chorkendorff, I.; Nørskov, J. K. *J. Am. Chem. Soc.* **2005**, *127* (15), 5308–5309.
- (47) Deb, S. K.; Chopoorian, J. A. *J. Appl. Phys.* **1966**, *37* (13), 4818–4825.
- (48) Bhosle, V.; Tiwari, A.; Narayan, J. *J. Appl. Phys.* **2005**, *97* (8), 083539–1–083539–6.
- (49) Greiner, M. T.; Helander, M. G.; Wang, Z. B.; Tang, W. M.; Qiu, J.; Lu, Z. H. *Appl. Phys. Lett.* **2010**, *96* (21), 213302–1–213302–3.
- (50) Shi, Y. F.; Guo, B. K.; Corr, S. A.; Shi, Q. H.; Hu, Y. S.; Heier, K. R.; Chen, L. Q.; Seshadri, R.; Stucky, G. D. *Nano Lett.* **2009**, *9* (12), 4215–4220.
- (51) Pentland, N.; Bockris, J. O.; Sheldon, E. *J. Electrochem. Soc.* **1957**, *104* (3), 182–194.
- (52) Conway, B. E.; Tilak, B. V. *Electrochim. Acta* **2002**, *47* (22–23), 3571–3594.
- (53) Markovic, N. M.; Grgur, B. N.; Ross, P. N. *J. Phys. Chem. B* **1997**, *101* (27), 5405–5413.
- (54) Skulason, E.; Karlberg, G. S.; Rossmeis, J.; Bligaard, T.; Greeley, J.; Jonsson, H.; Nørskov, J. K. *Phys. Chem. Chem. Phys.* **2007**, *9* (25), 3241–3250.
- (55) Skulason, E.; Tripkovic, V.; Bjorketun, M. E.; Gudmundsdottir, S.; Karlberg, G. S.; Rossmeis, J.; Bligaard, T.; Jonsson, H.; Nørskov, J. K. *J. Phys. Chem. C* **2010**, *114* (42), 18182–18197.
- (56) Chen, L. L.; Guay, D.; Lasia, A. *J. Electrochem. Soc.* **1996**, *143* (11), 3576–3584.
- (57) Vijh, A. K. *J. Phys. Chem.* **1968**, *72* (4), 1148–1156.
- (58) Belanger, A.; Vijh, A. K. *J. Electrochem. Soc.* **1974**, *121* (2), 225–230.
- (59) Kautek, W.; Gerischer, H. *Surf. Sci.* **1982**, *119* (1), 46–60.
- (60) Bahl, O. P.; Evans, E. L.; Thomas, J. M. *Proc. R. Soc. London, Ser. A* **1968**, *306* (1484), 53–65.
- (61) Chianelli, R. R.; Ruppert, A. F.; Behal, S. K.; Kear, B. H.; Wold, A.; Kershaw, R. *J. Catal.* **1985**, *92* (1), 56–63.
- (62) Roxlo, C. B.; Deckman, H. W.; Gland, J.; Cameron, S. D.; Chianelli, R. R. *Science* **1987**, *235* (4796), 1629–1631.
- (63) USCAR Fuel Cell Tech Team Cell Component Accelerated Stress Test Protocols for PEM Fuel Cells; Department of Energy: Washington, DC; http://www1.eere.energy.gov/hydrogenandfuelcells/pdfs/component_durability_may_2010.pdf.
- (64) Chen, Z.; Jaramillo, T. F.; Deutsch, T. G.; Kleiman-Schwarsstein, A.; Forman, A. J.; Gaillard, N.; Takanabe, K.; Heske, C.; Sunkara, M.; McFarland, E. W.; Domen, K.; Miller, E. L.; Turner, J. A.; Dinh, H. N. *J. Mater. Res.* **2010**, *25* (1), 3–16.